Numerical Investigation of Tsunami Bore Effects on Structures, Part II: Effects of Bed Condition on Loading onto Circular Structures

Nora Asadollahi

Formerly MSc Student, Department of Civil Engineering, University of Ottawa, 161 Louis Pasteur, Ottawa, ON, Canada, K1N 6N5. E-mail: nasad010@uottawa.ca

Ioan Nistor

Professor, Department of Civil Engineering, University of Ottawa, 161 Louis Pasteur, Ottawa, ON, Canada, K1N 6N5. E-mail: inistor@uottawa.ca

Abdolmajid Mohammadian

Professor, Department of Civil Engineering, University of Ottawa, 161 Louis Pasteur, Ottawa, ON, Canada, K1N 6N5. E-mail: amohamma@uottawa.ca

Abstract

In this paper, a multi-phase three-dimensional numerical reproduction of a large-scale laboratory experiment of tsunami-like bore interaction with a surface-piercing circular column is presented. The numerical simulation is conducted using OpenFOAM. A dam-break mechanism is implemented in order to generate tsunami-like bores. The numerical model is validated using the results of experiments performed at the Canadian Hydraulics Center of the National Research Council (NRC-CHC) in Ottawa, Canada. Unsteady Reynolds Averaged Navier-Stokes (RANS) equations are used in order to treat the turbulence effects. The Shear Stress Transport (SST) k-ω turbulence model showed a high level of accuracy in replicating the bore-structure interactions. A scaled-up domain is used to investigate the influence of bed condition in terms of various downstream depths and roughnesses. Finally, a broad investigation on bore propagation characteristics is performed. The stream-wise forces exerted on the structural column as well as the bore velocity are compared and analyzed for smooth, rough, dry and wet beds with varying depths.

Keywords: Hydrodynamic force, Bed condition, Hydraulic bore, OpenFOAM

1. Introduction

Recent tsunami events have shown that these phenomena can be devastating and cause catastrophic human losses as well as vast damage to coastal infrastructure. The 2011 Tohoku tsunami, induced by a subduction earthquake (M_W 9.0), resulted in around 20,000 fatalities and 264,468 partially or fully collapsed buildings. It was reported by the government of Japan as one of Japan's most expensive natural disasters, with damage costs of over $217 billion. The inundation height ranging from 10m to 38m, while a maximum run-up height of around 41 m was reported (EERI, 2011). Mikami et al. (2012) conducted a field survey after the 2011 Japan tsunami and reported extensive reinforced concrete building damage in coastal areas. The tsunami intruded several kilometers inland, and there were not enough high-ground sites for evacuation. Yeh (2013) reported that the major reasons for the extensive structural damage during the 2011 Japan tsunami were unexpected inundation depth, scouring effects, high bore velocities and buoyancy forces.

Based on these points, the importance of revising and developing building guidelines to protect buildings against tsunami loading was revealed. The present paper is a part of an ongoing interdisciplinary research program which was started at the University of Ottawa in order to improve the design guidelines for estimating tsunami-induced forces. One of the major factors in bore propagation characteristics is the effects of bed condition. As tsunami waves are generated by abrupt vertical motions of the seabed in deeper water, one or a series of waves can form. These waves advance can towards coastal areas, and once they reach shallow water areas, owing to shoaling effects, break into a series of turbulent bores and eventually intrude onto inland regions as a hydraulic bore. Generally, the first tsunami wave propagates over dry land (dry bed condition) while subsequent waves may intrude over the flooded coastline before full recession of the first wave (i.e., wet bed condition). Pervious research has shown that the presence of a water layer on the bed can affect a tsunami bore's characteristics. In addition, the bed condition (e.g., smooth versus rough) also affects bore propagation and the resulting forces acting on coastal structures.

In the present study, a three-dimensional multiphase numerical model is applied in order to study tsunami bore impacts on surface-piercing structures. Chanson (2006) demonstrated that tsunami-induced and dam-break waves are similar in their characteristics. Here, the experimental setup used by Nouri et al. (2010) is used to validate the efficiency of the numerical model. A dam-break approach is used in order to generate the hydraulic bore. In this approach, the still water behind the gate is released suddenly. The main objective of this study is to investigate and analyze the effects of bed conditions (e.g., wet, dry, smooth or rough) on velocity fields, bore depths and the resulting pressure and forces exerted on structures. Flows around circular and elliptical columns are studied and analyzed. Moreover, in order to equate the similarity between the model and the real-world prototype, the numerical model is scaled up. To do so, the model sidewalls are moved away so that they no longer affect the resulting force due to blockage effects.

Since the current paper's scope is tsunami-like bore-structure interactions, some relevant numerical and experimental works in the literature are presented here. Numerous studies have been done on both submerged and free surface flows around circular columns for steady and unsteady flows. A numerical study using a large eddy simulation (LES) was performed by Kawamura et al. (2002) to study the flow moving around a free surface-piercing circular column in order to investigate the effects of different values of Froude numbers.

Yu et al. (2008) examined the different ranges of Froude and Reynolds numbers using a two-phase LES numerical approach, and the authors reported that drag force increased by increasing the Reynolds number and decreased slightly by increasing the Froude number. Sadeque et al. (2008) experimentally studied the hydraulics of flow around a circular structure in an open channel. The authors examined the effects of different levels of submergence as well as a surface-piercing structure on the resulting bed shear stress and vortex-shedding in the wake of the structure.

Extensive studies have been performed to investigate dam-break wave interactions with surface-piercing structures on both dry and wet bed conditions. A laboratory experiment was conducted by Ramsden (1996) in two separate wave tanks to study turbulent bore interactions with a vertical wall. A comparison between dry and wet bed conditions demonstrated that bore depths, run-ups and forces acting on vertical walls for the wet bed condition exceeded those for the dry bed. Arnason (2005) studied broken tsunami bore interactions with circular columns of different sizes considering the initial downstream depth, $h_d = 0.02$ m, and based on the results, the obtained forces are lower for the column with smaller diameter. Moreover, the wake effects and run-up heights were minimal for smaller circular columns. For the case of large circular columns, the author reported that the hydrodynamic force significantly overshoots the initial impulsive force, especially for higher bore depths. This is attributable to the higher water build-up behind the larger circular columns.

Many numerical studies have investigated the influence of bed conditions on tsunami-bore impacts on structures. Gomez-Gesteira and Dalrymple (2004) studied dam-break wave interactions with a tall vertical structure using the smooth particle hydrodynamics (SPH) method. The maximum force exerted on the column for the dry bed condition occurred at lower elevations, while for the wet bed condition it occurred at higher elevations.

Leal et al. (2006) performed a series of experimental tests to investigate the magnitude of dam-break bore front celerity for different bottom frictions and downstream bed conditions (wet or dry). The authors argued that the bore front celerity decreases as the ratio of h_d/h_u increases until the bore front celerity no longer changes with the increase in h_d. Crespo et al. (2008) investigated the dam-break bore evolution over wet and dry beds using a two-dimensional SPH method. The authors introduced two dissipation mechanisms, including wave-breaking and bottom friction, as major factors causing dissipation over wet and dry bed conditions, respectively.

St-Germain et al. (2012) studied tsunami-like bore structure interactions advancing over wet and dry bed conditions using the SPH method. Based on their results, the bore front celerity was notably smaller for the wet bed case due to the resistance imposed by the water layer downstream. Douglas and Nistor (2014) studied the effect of bed conditions on the interaction of tsunami-like bores with a square structure using a three-dimensional multiphase numerical model. The results showed a substantial change in bore characteristics as the downstream bore depth (h_d) increased. The authors observed deeper and steeper bore fronts for wet bed conditions; however, the shape of the bore front did not change substantially as downstream depth increased. Wei et al. (2015) studied the dynamic interaction of a bore with bridge piers using the SPH method. The results showed that the dimensionless width of the flume is proportional to the hydrodynamic force and bed shear stress. In Section 2, the governing equations and numerical model are introduced. The comparison between the numerical results and laboratory measurements is performed for force, pressure and bore surface elevation in Section 3. In Section 4, the results of the bore structure interaction and the obtaining force, pressure, velocity fields and bore surface elevation are presented using

scaled-up computational domain. Finally, in Section 5, conclusions and suggested future works are presented.

2. Numerical method

2.1. Description of OpenFOAM

In order to solve three-dimensional Reynolds Averaged Navier-Stokes equations (RANS), OpenFOAM (Open Field Operation and Manipulation) includes a solver called *interFoam* for incompressible two-phase flows. Solvers represent solution algorithms and Partial Differential Equations (PDEs) developed to deal with relevant continuum mechanics problems. The RANS equations can be applied to a variety of coastal problems, and the Finite Volume Method (FVM) is implemented in order to discretize the governing equations. The *interFoam* solver tracks the water surface elevation using the Volume of Fluid (VOF) method. Since the program language, C++, is object-orientated and the code and mathematical syntax are mostly similar, it provides a user-friendly environment for modification and development of the source code.

2.2. Governing equations

The RANS equations which contain mass conservation and momentum equations for incompressible fluids are used by OpenFOAM, and as expressed by Rusche (2002):

$$\nabla \cdot \mathbf{U} = 0, \tag{1}$$

$$\frac{\partial \rho \mathbf{U}}{\partial \mathrm{t}} + \nabla \cdot (\rho \mathbf{U}\mathbf{U}) - \nabla . (\mu_{\mathrm{eff}} \nabla \mathbf{U}) = -\nabla \mathrm{p} + \nabla \mathbf{U} . \nabla \mu_{\mathrm{eff}} - \mathrm{g} . \mathbf{X} \nabla \rho + \sigma \kappa \nabla \alpha \tag{2}$$

where ρ, U, p ,g , X, σ, κ and α are the density, velocity vector, pseudo-dynamic pressure, gravity acceleration, position vector, surface tension coefficient and the interface curvature and indicator function, respectively. The bolded components represent the vector field, and κ is defined as

$$\kappa = \nabla \cdot \frac{\nabla \alpha}{|\nabla \alpha|} \tag{3}$$

The effective dynamic viscosity μ_{eff} is defined as

$$\mu_{\mathrm{eff}} = \mu + \rho \upsilon_{\mathrm{turb}} \tag{4}$$

where υ_{turb} and μ are the turbulent kinetic viscosity and molecular dynamic viscosity, respectively.

The terms in (2) are specified in a form where the terms on the left-hand side of (2) are considered to build the coefficient matrix and those on the right-hand side are used as an independent terms of equations (Higuera et al., 2013).

In order to capture the free surface elevation, the volume of fluid technique is implemented in OpenFOAM. This method simplifies the measurement of complex free surfaces and is computationally less expensive. An indicator phase function (α) is defined in order to measure the occupied volume per unit of each mesh cell (Berberovic et al. 2009). In the present study, a two-phase flow (water and air) is presented; therefore, $\alpha = 1$ indicates that the cell is filled with water and $\alpha = 0$ indicates that the cell is

empty. Finally the values between 0 and 1 represent the interface. Each property of the fluid (∅) can be measured by weighting them using the VOF method.

$$\emptyset = \alpha\ \emptyset_{\text{water}} + (1 - \alpha)\emptyset_{\text{air}} \quad (5)$$

An additional advection equation should be solved in order to track the water surface movement, which is described by:

$$\frac{\partial \alpha}{\partial t} + \nabla.(U\alpha) + \nabla.U_c\ \alpha(1 - \alpha) = 0 \quad (6)$$

where U_c denotes the compression velocity. The value of α must be limited to between 0 to 1 in order to maintain the sharp interface and avoid numerical diffusion in (6), and in order to do so, an artificial compression term $\nabla.U_c\ \alpha(1 - \alpha)$ is used (Weller, 2002).

2.3. Turbulence modelling

In turbulent flows governed by Navier-Stokes equations, each quantity of flow can be decomposed into a mean and fluctuating part. The RANS equations (Section 3.2) are basically obtained through the mean flow variables of the governing equations. A new term, Reynolds stresses, which represents the nonlinearity (turbulent fluctuations) is introduced in the RANS equations. The turbulent stress may be estimated based on the Boussinesq eddy viscosity concept. To predict the effects of turbulence, different turbulence models are used in OpenFOAM. The variable turbulent kinetic viscosity (υ_{turb}) introduced in (2) is obtained by choosing the turbulence model. The turbulent dissipation is then simulated using the turbulent viscosity added to the molecular viscosity (4).

In the current work, the k–ω SST (Shear Stress Transport) turbulence model is used to model the turbulence. Menter (1994) blended the k-ε (Launder and Spaulding, 1974) and k-ω (Wilcox, 1998) models to obtain a new model with the best characteristics of each. To do so, the transformation from the k-ε model into the k-ω is performed. The k-ε model gives accurate results for free shear layers far from surface; however, this model does not perform well within the boundary regions and simulation of the flow separation. This can be compensated for by using the k-ω model in the inner regions. Some significant deficiencies of the k-ω model are its less accurate performance in the wake of the boundary layer and its inaccurate prediction of asymptotic behavior of the turbulence near the wall regions. del Jesus et al. (2012) were amongst the first to implement the k–ω SST turbulence model in wave-structure interaction problems. For more information about the basic equations of the k–ω SST model, the reader is referred to Menter (1994).

2.4. Initial and boundary conditions

The initial and boundary conditions (BC) of the numerical domain are specified in order to achieve the actual physical interpretation. Generally, two types of boundary conditions are prescribed, including the Fixed Value Boundary Condition (Dirichlet) and Fixed Gradient Boundary Condition (Von Neumann). The Fixed Gradient Boundary Condition defines the gradient of the field variable normal to the boundary, while the Fixed Value Boundary Condition defines the value of an independent field variable at the boundary. A no-slip boundary condition for velocity (u) is adopted, and zero gradient pressure (p) and phase fraction (α) are assigned for at the flume's walls and bed.

The physical behavior of the near-wall areas is different from the other parts of the flow region. Launder and Spalding (1974) introduced a new term in momentum equations which compensates for the increased

turbulent viscosity at the transitional and wall regions. The law of the wall is used to treat other turbulence components (k, ω, ...). In this way, the turbulence transport equations are not solved near the wall region. The wall boundary condition can be specified for each patch in OpenFOAM. Two types of wall function, namely nutWallFunction and nutRoughWallFunction, are used in the present work for hydraulically smooth and rough bed conditions, respectively, to specify the turbulent viscosity effects. The roughness characteristics can be easily adapted in the OpenFOAM turbulent eddy viscosity directory. The velocity and the phase fraction at the flume's outlet are assigned as zero gradients, and the pressure is set to be a fixed value. The atmospheric boundary condition at the flume's top face is adopted as similar to that at the flume's outlet (Rusche, 2002).

The phase fraction (α) is set to 1 in parts of flume filled with water at the reservoir during the initial time before releasing the impounded water (h_u). For the wet bed condition cases at the flume downstream, the same phase fraction ($\alpha = 1$) is applied up to the downstream water depth (h_d). For the remaining parts of the flume, $\alpha = 0$ is assigned, since it is filled with air. Furthermore, the initial velocity and pressure are set to zero and the turbulence parameters are assigned to small initial values for the sake of convergence of the initial iteration.

3. Validation of the model

3.1. Physical experiments of Nouri et al. (2010)

The physical experiments were conducted in a 10.6 m long, 2.7 m wide, 1.4 m high flume at the Canadian Hydraulic Center of the National Research Council (NRC-CHC), located in Ottawa, Canada. The schematic plan view of the flume is shown in Fig. 1. A variable-pitch pump is used in order to adapt the discharge amount (0 to 1.7m^3/s) inside the flume. The flume was fabricated from stainless steel, with two glass side windows at the location of the structure to providing video capture of the flow. The still water behind the swinging gate was suddenly released based on the dam-break mechanism, and highly turbulent bores advanced downstream. The gate removal duration based on the video recording was estimated at about 0.25sec to 0.3sec. The experimental test was performed for several impounded water depths (h_u=0.50m, h_u=0.75m, h_u=0.85m and h_u=1.0m). To avoid water leakage into the downstream area, some rubber water-stops were positioned on the upstream side of the swinging gate.

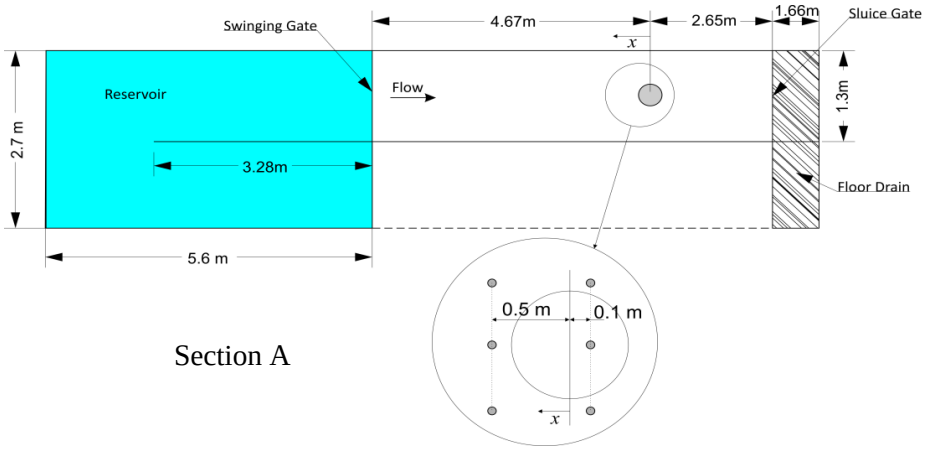

Fig. 1 Plan view of the physical experiment, Section A: layout of WGs in the absence of column

Different structural cross-sections were used in the experiments; however, the circular structure is of interest in the present study. The circular column was fabricated of polyvinyl chloride (PVC) with a 320mm outer diameter, 9mm thickness and 700mm height. Seven wave gauges (WG, capacitance type) with a sampling rate of 1 kHz were positioned inside the flume at the desired location in order to measure the water surface elevation. The vertical distances of the WGs were approximately 10 to 20mm from the flume bottom. In order to measure the stream-wise force exerted on the circular column, a multi-component dynamometer (AMTI MC6 series) was utilized. The column was attached to the upper plate of the dynamometer, and the applied forces and moments were converted to voltages and recorded using the data acquisition system. Steel mounts were attached and bolted to both the circular column and the dynamometer. The sampling rate was set to 1 kHz. The pressure exerted on the column was captured using the differential pressure transducers (Honeywell model PK 80083) with a waterproof sensor with a capacity of 15.1kPa. Ten 5mm-diameter holes were mounted on the upstream side of the circular column with the distance of 50mm.

3.2. Validation of the numerical experiment

3.2.1. The Computational Domain

The precise geometry of Nouri et al.'s (2010) physical experiment was replicated here. The general configuration of the numerical domain is shown in Fig. 2. The flume drain is simulated numerically to avoid the formation of backflow. Impounded water depths of h_u=0.50m and h_u=0.85m were chosen to examine the capability of the numerical simulations. After releasing the impounded water, the bores advanced into the flume downstream and impacted the column. The net stream-wise force exerted on the column and the water surface elevation and pressure time histories were measured at every time step. An unstructured mesh discretization was used for each simulation using ABAQUS in order to save computational cost. The total number of mesh cells was 1.6 million. The computational time needed to simulate 8sec of the physical experiment was approximately 5.5 days using 2 processors (3.60GHz). In order to achieve accurate results, finer mesh sizes were adopted in the vicinity of the column. The mesh resolution near the column was chosen to be 1x1x1.5 cm in the x, y and z directions, respectively. This discretization grows gradually farther away from the column. In order to capture the turbulence effects around the structure, the mesh resolution was kept fine at radius of 1.2 m around the circular column.

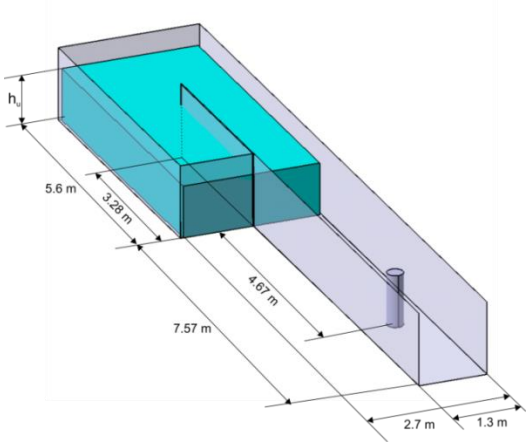

Fig. 2 Computational Domain

3.2.2. Sensitivity Analysis

The results of the sensitivity analyses of the turbulence model are presented in Fig. 3. First, a sensitivity analysis of the turbulence model was performed using three different RANS turbulence models: k–ω SST, realizable k-ε and k-ε, and the time histories of the stream-wise forces exerted on the circular column are compared for these models. As shown in Fig. 3, the forces obtained from the k–ω SST turbulence model give the best match with Nouri et al.'s (2010) experimentally captured forces. A slight discrepancy can be observed between 2.0 sec to 3.0 sec in the time history of the forces obtained by the k–ω SST turbulence model; however, the overall agreement between the numerical simulation and experimental results for the stream-wise forces is reasonable. In contrast, for the two other turbulence models, the captured stream-wise forces from the numerical simulation over-predict the stream-wise forces.

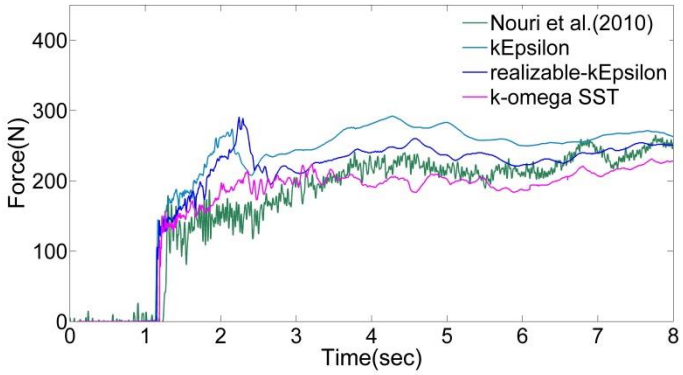

Fig. 3 Sensitivity analysis of turbulence models

3.2.3. Validation results

A comparison of the numerical time histories of the stream-wise force with the experimentally captured force is displayed in Fig. 4.The results show a good level of agreement between the time histories of the stream-wise forces for the numerical and experimental measurements for the impounded water depth h_u**=0.50m**.

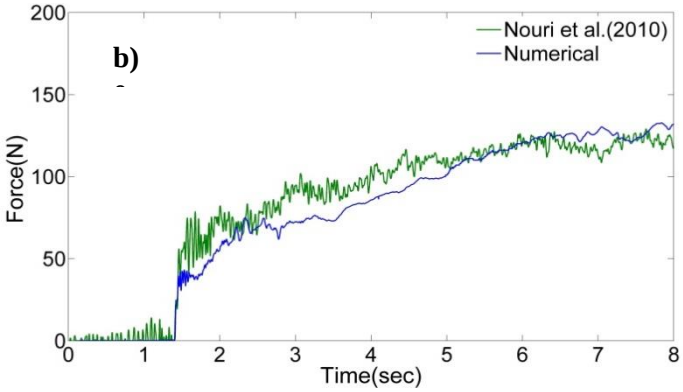

Fig. 4 Time histories of stream-wise force for impounded water depths h_u**=0.50m**

In general, the overall trends of the stream-wise force for the numerical simulation of the case h_u=0.55m show a reasonable agreement. In St-Germain et al.'s (2012) numerical study, the single-phase smoothed particle hydrodynamics (SPH) numerical model is implemented. The resulting stream-wise force exerted on the circular column show significantly higher values compared to the experimental force. Generally, the validation results for the force show that the present model is capable of accurately computing the stream-wise force acting on the structural column as compared to the SPH model.

Moreover, the time histories of the pressure are also presented in Fig. 5 for different vertical elevations on the upstream side of the column. The numerical simulations of pressure are compared with the experimental measurements obtained from pressure transducers (PTs) located at 5cm (PT5) and 25cm (PT25) above the channel bottom. During the initial impact, some discrepancies due to numerical oscillation are occurred to capture the impulsive shock pressure at PT5. However, later, in the quasi-steady state, a fair level of agreement can be observed. As the vertical distance above the flume channel increases, the magnitude of the impulsive pressure decreases. This can be seen in Fig. 5b for PT25. Although a slight drop in the numerical time history of the pressure can be observed after 5.5sec, the overall trend follows the experimental measurements.

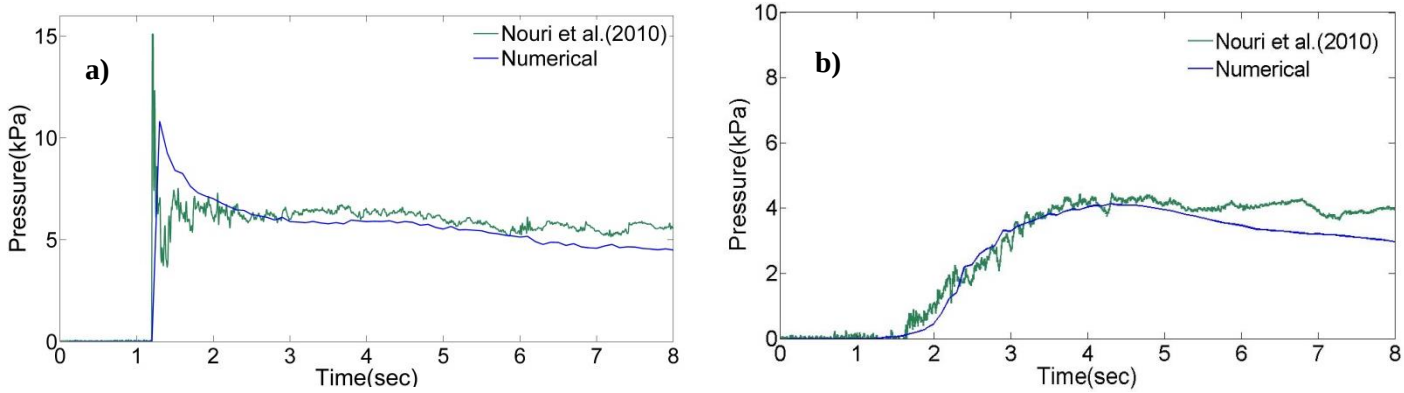

Fig. 5 Time histories of pressure for PT for impounded water depths h_u=0.85m a) PT5 b) PT25

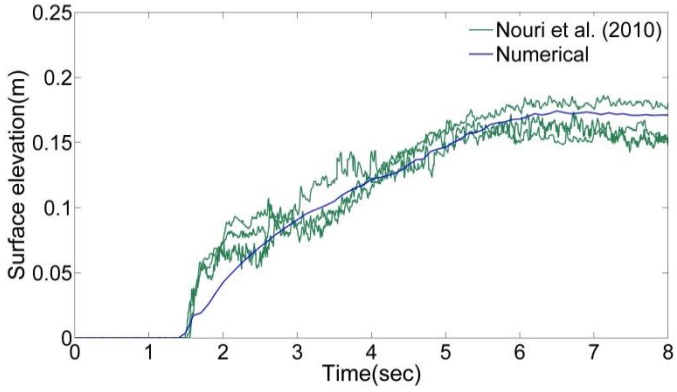

Fig. 6 Comparison of numerical and experimental temporal variations of water surface elevation for h_u=0.50m at $x = +0.1$

A quantitative comparison of the temporal variations in water surface elevation for the unobstructed flow condition is presented in Fig. 6 for WG1, WG2, and WG3. As shown in Fig. 1, the WGs are located in a row at $x = +0.1$ in the absence of a structure. Although the numerical model shows some discrepancies in the first moments of simulation ($t = 1.5\text{sec}$), for the rest of the simulation, the numerical model replicates fairly the experimentally captured water surface elevation. For numerical WGs, since the results of all the WGs are the same, only one of them is displayed here.

4. Results and discussions

4.1. Computational domain

Two computational domains were simulated for a better understanding of bore-structure interactions in a dry bed condition: (i) circular column, and (ii) elliptical column. The minor axis of the elliptical column is kept the same as the circular column's diameter, and the major axis is considered as twice that of the minor axis in the direction of flow. Moreover, the influence of bed condition on flow propagation characteristics and the resulting force exerting on the circular column is investigated. For this reason, numerical simulations are performed for dry and wet bed conditions, as well as considering bottom friction. For the dry bed case, smooth, sand and asphalt beds are examined. In order to assign the bottom friction, the roughness height (k_s) can be easily defined, as discussed in Section 2.4. For the wet bed condition, three cases are modeled, which include h_d=0.050h_u, h_d=0.30h_u and h_d=0.50h_u. All cases are examined for h_u= 550mm and h_u= 850mm. In order to avoid flow blockage affecting the resulting forces exerted on the column, the flume width is increased. The blockage effect of the sidewalls forms a subcritical wave which propagates upstream. Arnason et al. (2009) argued that the formation of bow waves is caused by bore run-up on the sidewalls upstream of the column. This results in water build-up behind the structural column in a narrow channel and may affect the resulting force. The blockage ratio is defined as the ratio of the column width to the flume width. Wei et al. (2015) conducted a numerical replication of Arnason et al.'s (2009) experimental work; for example, for the case of a circular column, the authors performed additional simulations by increasing the flume width by 50% (BR=16%) and 100% (BR=12%) and compared the resulting hydrodynamic force with the value obtained from the original setup (BR=23%). Based on their results, the wider the flume was, the lower the values for hydrodynamic force were obtained. This was also observed by St-Germain et al. (2014).

In the present study, the BR=7% is considered conservatively. In order to achieve this ratio, the computational domain is expanded. The general configurations for the dry and wet bed conditions are shown in Fig 7. The drain was simulated in order for the water to easily leave the computational domain. For the wet bed cases, in order to simulate the motionless water on the downstream side of the channel floor, a partition equal to the height of the water layer downstream (h_d) is modeled, preventing the downstream water from leaving the computational domain. The circular structural column is positioned downstream at 4.92m from the reservoir in order to ensure that the bore will fully develop. The circular column's diameter and height are taken as 0.32 m and 1.0 m, respectively. The number of grid cells is approximately 2.3 million. The same mesh resolution and quantities are considered in the vicinity of the structure, as described in Section 3.2.1.

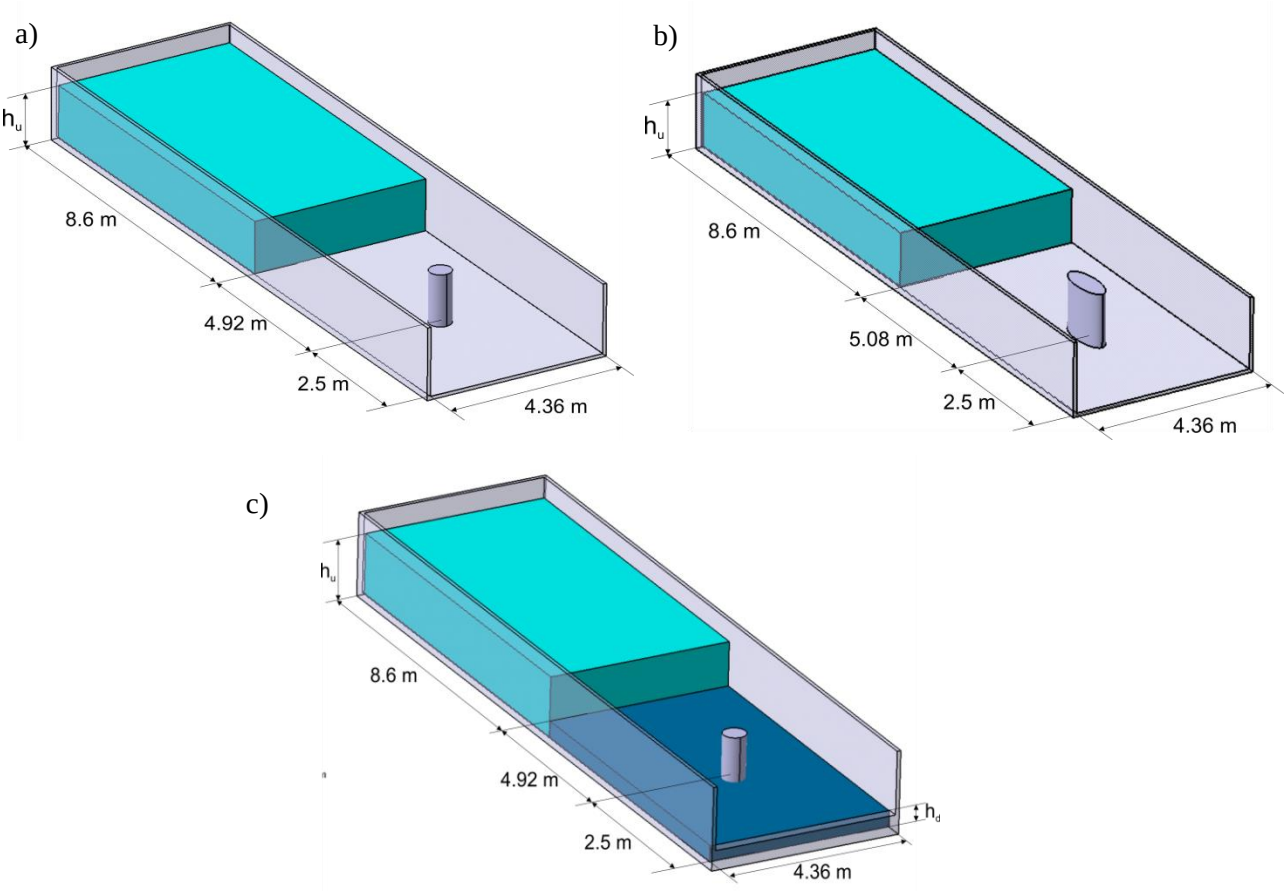

Fig. 7 Computational domains: a) circular column over dry bed; b) elliptical column over dry bed; c) circular column over wet bed

4.2. Comparison of force action on circular vs. elliptical columns

The time histories of the stream-wise force for an impounded water depth of h_u= 550mm are presented in Fig. 8a for both the circular and elliptical structures. Moreover, in Fig. 8b the bore run-ups on the upstream side of the columns are presented. The sharp curves at some moments could be attributed to numerical diffusion. As can be observed, the hydrodynamic forces exerted on the elliptical column are drastically lower with respect to the circular column. Although the projected width subjected to the flow is equal for both columns (i.e., diameter of the circular column), it appears that the shape of the curvature at the upstream side of the elliptical column smoothly splits the flow and redirects it around the column. Bore run-up on the column upstream is almost negligible at this case. The overall comparison between the run-up elevations indicates that a higher elevation for the circular column was captured relative to the elliptical column, especially at the initial moments after impact (Fig. 8). However, after around 6.0 sec, the resulting force converged for both structural columns.

The evolution of the bore around the columns as well as the measured force exerted on the columns are studied at some key moments. The impulsive force occurred momentarily after impact at t=1.6sec (red points, A, in Fig. 8). Comparing the bore run-ups on the upstream face of both structural columns at this time shows a lower elevation for the elliptical column, and as a result, less impulsive force occurred. Afterwards, the bore splashed back after the initial run-up (purple points, B) and formed a roller surface around the column. These moments can be observed after t=2.1sec in Fig. 9 and after t=2.6sec in Fig. 10 for the circular and elliptical columns, respectively. Unlike in Arnason et al.'s (2009) experimental study, the maximum force (heap) did not occur at the moment of run-up collapse, which was referred to as "bow wave" in their study.

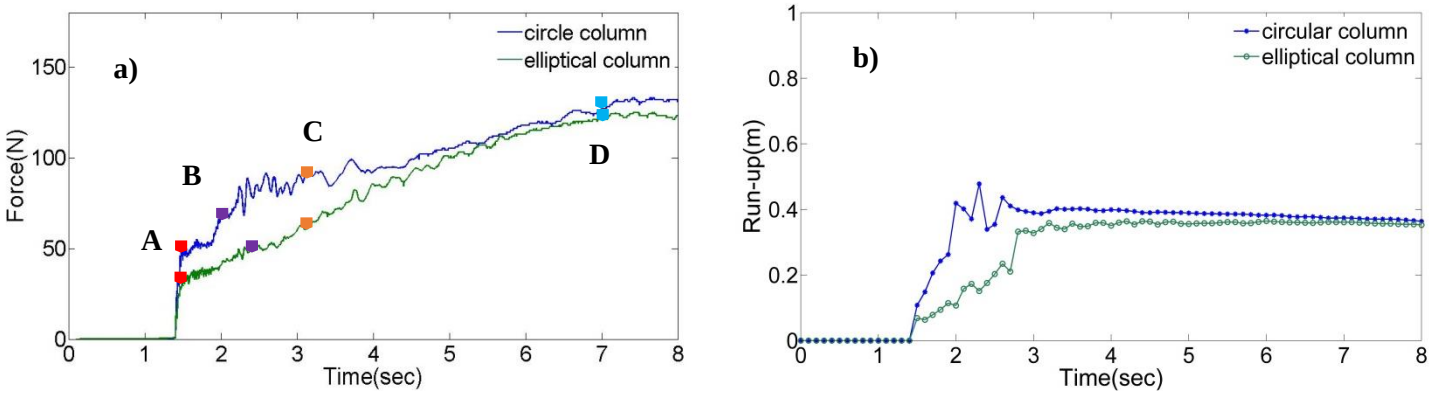

Fig. 8 Time histories of the circular vs. elliptical columns for h_u=550mm: a) stream-wise force acting on the columns; b) bore run-up on the upstream side of the columns

The quasi-steady state begins approximately after 3.2sec for both columns. It appears that the combination of high velocity and bore depth leads to the maximum hydrodynamic force (orange points, C). The resulting force grew until 7.0sec when it finally remained constant. By this time, the wave advancing upstream induced by obstruction can be clearly observed. The surface roller has almost disappeared by this time (blue points, D).

The formation of the wake and its structure is also highlighted in order to better analyze the force exerted on the column. The wake formed after 2.1 sec at a position about two times the diameter of the column in the downstream direction. For the elliptical column, the bore rejoined after 2.2 sec at a position about one-and-a-half times the ellipse's major axis downstream and led to wake formation. The formation of a rooster-tail in the wake of the structure was evident at the centerline of the flume.

As shown in Fig. 9 and Fig. 10, after 3.2sec the bore in the wake of the columns is completely developed as the surface roller redirects around the column and fills the downstream part of the flume. This results in a vortex downstream of the column. At this time, the wake is highly turbulent and contains a high amount of air entrainment.

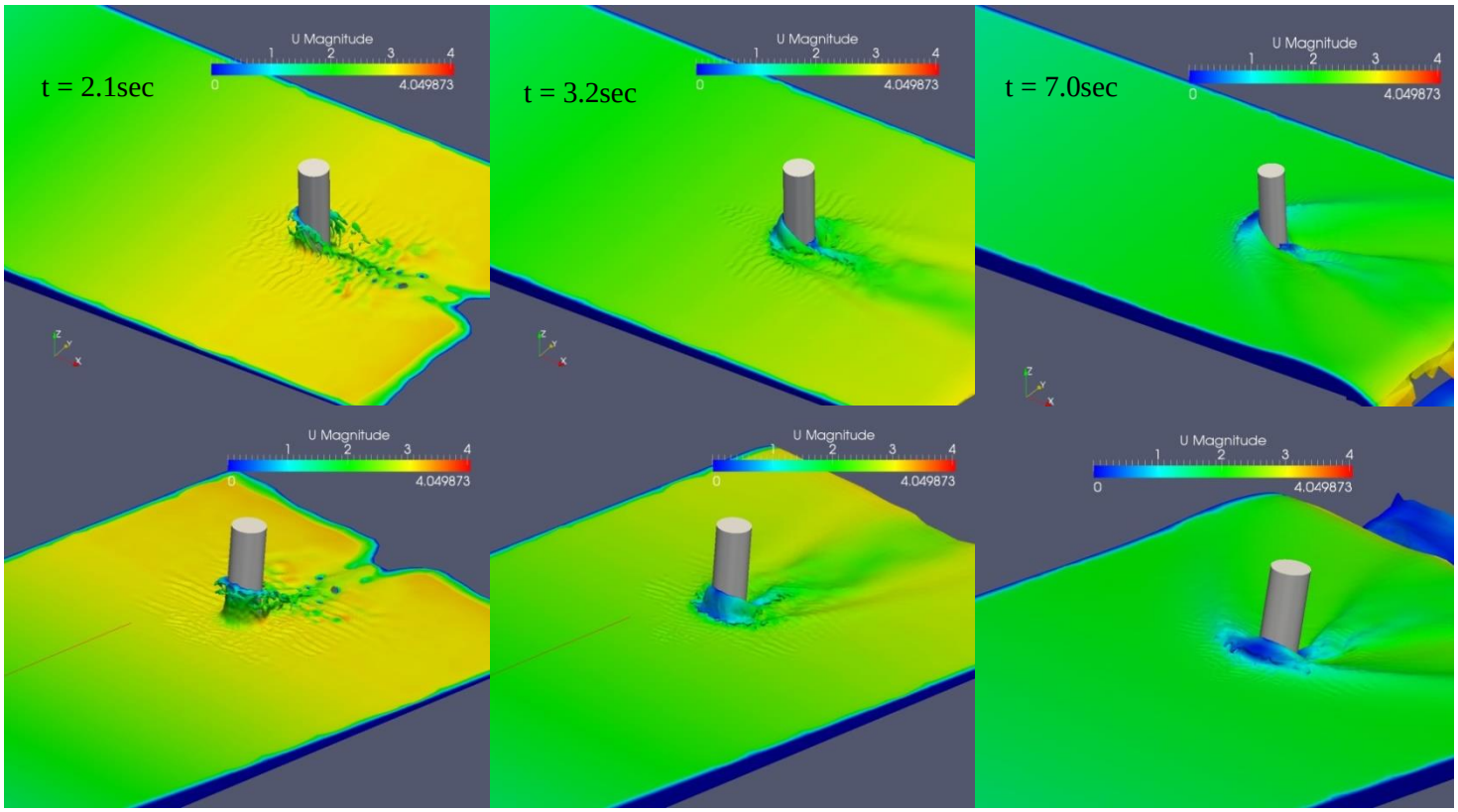

Fig. 9 Snapshots of bore impinging on the circular column at some key moments

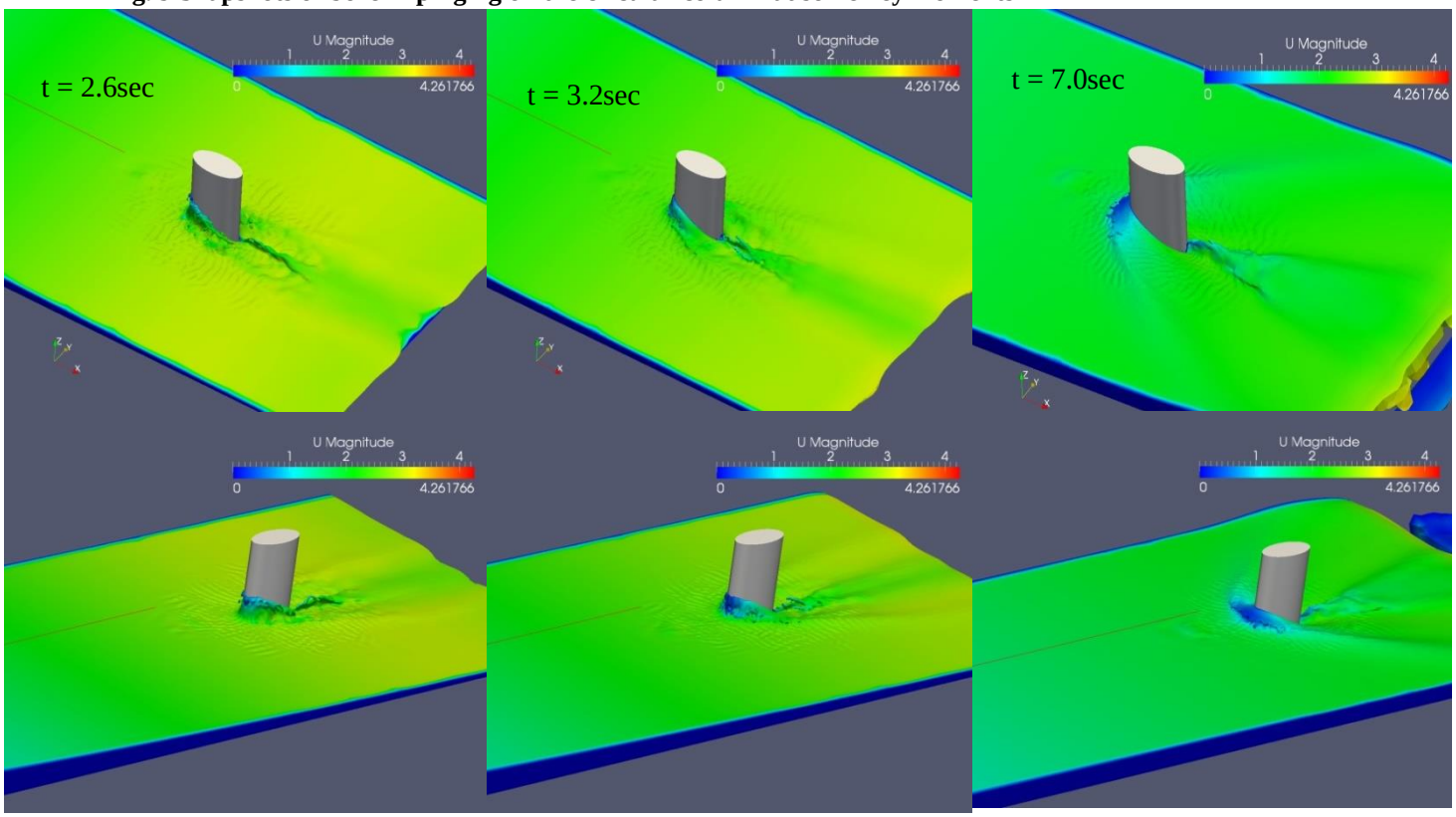

Fig. 10 Snapshots of bore impinging on the elliptical column at key moments

4.3. Effects of bed condition

Generally, tsunami waves intrude onto inland areas in the form of highly turbulent hydraulic bores. The first tsunami wave usually inundates inland areas over a dry bottom, referred to as a "dry bed condition", while the second and/or third waves of a tsunami may advance onto the inland area before the first wave's flood recedes. This scenario is referred to as a "wet bed condition". As reported in the literature, the presence of still water layer (h_d) on the flume bottom can drastically influence propagation development. In this section, bore propagation characteristics for both the wet and dry bed conditions are compared and discussed. Also, the resulting forces and pressures are presented for all tested downstream water depths. In this section, the influence of bed conditions for downstream to upstream water depth (h_d/h_u) is investigated for h_d/h_u as 0.05, 0.3 and 0.5.

4.3.1. Bore characteristics

A comparison between a dam-break analytical solution and a numerically obtained bore profile is presented here. Chanson (2009) developed a simple analytical solution for dam-break waves in the resistance-dominated wave tip region for both dry horizontal and sloped beds using shallow water equations. The bed friction was considered using the Darcy-Weisbach friction factor (ƒ). In Fig. 11, the X axis corresponds to the flume's length, and h represents the water surface elevation. As shown in Fig. 11, good agreement can be observed between the numerical model presented here and Chanson's (2009) analytical solution for the dry bed condition.

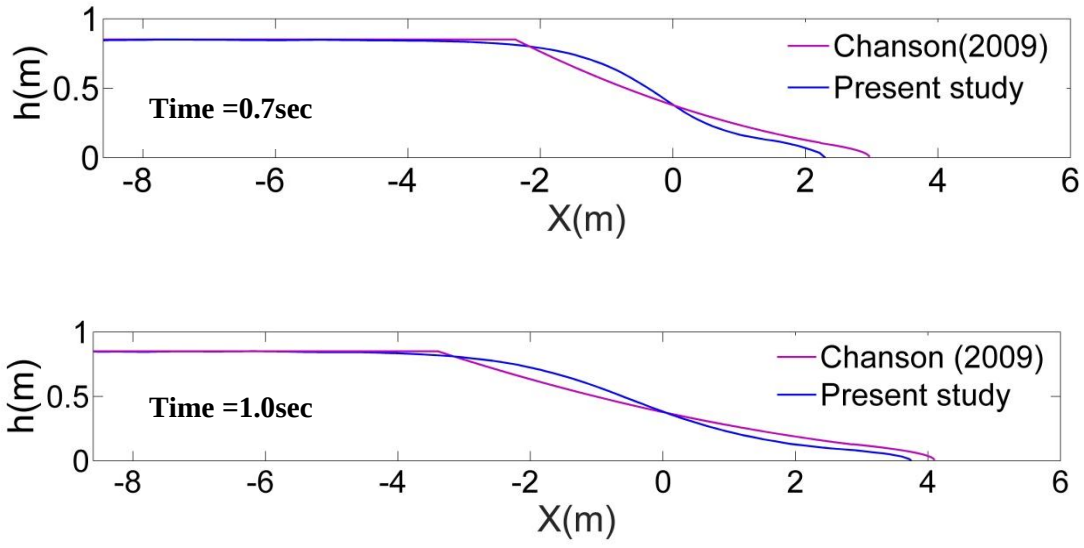

Fig. 11 Comparison of bore profile for the numerical model and Chanson's (2009) analytical solution

Furthermore, a comparison between the depth-averaged velocity for all tested downstream depths as well as the dry bed is presented in Fig. 12a. The velocities were measured at the upstream side of the column further from the stagnation region. The presence of a water layer downstream causes resistance to the propagation of the incoming bore. Therefore, as expected, the bore front velocity decreases as the

downstream depth increases, owing to energy dissipation. Moreover, a delay in the bore front arrival is observed as the downstream depth increases. As the downstream depth increases, a significant drop in bore front velocity occurs; however, for both the dry bed and wet bed conditions, with h_d/h_u as 0.05 (h_d=2.75cm), the depth-averaged velocities converge further after 3.0sec in the quasi-steady state. For higher downstream water depths (h_d/h_u as 0.3, (h_d=16.5cm) and h_d/h_u as 0.5 (h_d=27.5cm), a considerable reduction in depth-averaged velocity occurs. This significant change in velocity is observable even in the quasi-steady state. According to Douglas and Nistor's (2014) numerical study, for downstream to upstream ratios (h_d/h_u) ranging from 0.0043 to 0.043, the same reduction in bore front velocity is observed, and in the quasi-steady state, the velocities eventually converge. This trend is not observed in this study for higher downstream depths (i.e., h_d/h_u more than 0.3). It seems that after a specific downstream depth (here h_d/h_u more than 0.3), the bore propagation characteristics will change markedly due to higher turbulence and energy dissipation.

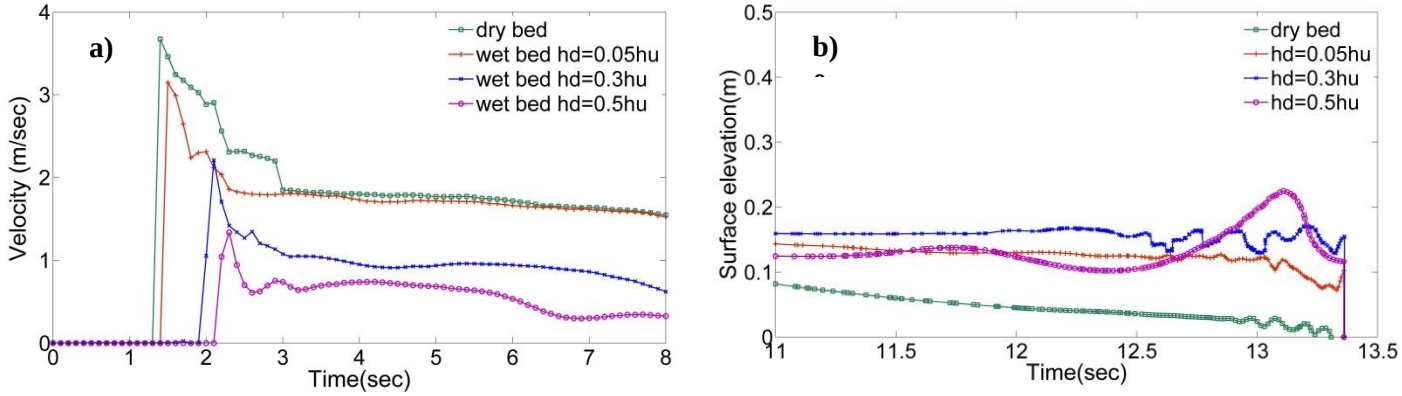

Fig. 12 Comparison between dry and wet bed conditions: a) depth-averaged stream-wise velocity of bore; b) bore front profile momentarily before impact

Fig. 12b shows a comparison of the bore profiles for all examined bed conditions momentarily before impact. All the bore profiles are measured and presented relative to the reference elevation of the still downstream water depth, since only these moving surface profiles contribute to the initial impact forces. For the case of h_d/h_u = 0.5, a distinct difference in the bore front profile appears. At the very front of the bore, an undulation in the bore surface forms prior to impact, followed by a less perceptible surface undulation behind. Interestingly, a lower water surface elevation was measured for the case of the h_d/h_u of 0.5 compared to the case of the h_d/h_u of 0.3. This can be attributed to a significantly lower total head for the case of h_d/h_u = 0.5 and a subsequent lower velocity. This lower head induces less kinetic energy. Moreover, it seems that a higher bed resistance is provided by higher (i.e., still water downstream. For the two wet bed conditions (h_d/h_u = 0.05 and 0.3), the relatively vertical bore front is measured with respect to the dry bed condition, and the general trend shows both a steeper and deeper bore front as the downstream water depth increases. The overall deeper and steeper slope for the downstream to upstream depth ratio of h_d/h_u = 0.5 may lead to the higher impulsive force at the initial impact, which will be discussed in the next section. The same bore front trend was reported by Janosi et al. (2004) and Crespo et al. (2008). Janosi et al. (2004) observed higher air-entrained bore fronts, unstable jets and wave-breaking for dam-break flows moving over a wet bed channel in their experimental study.

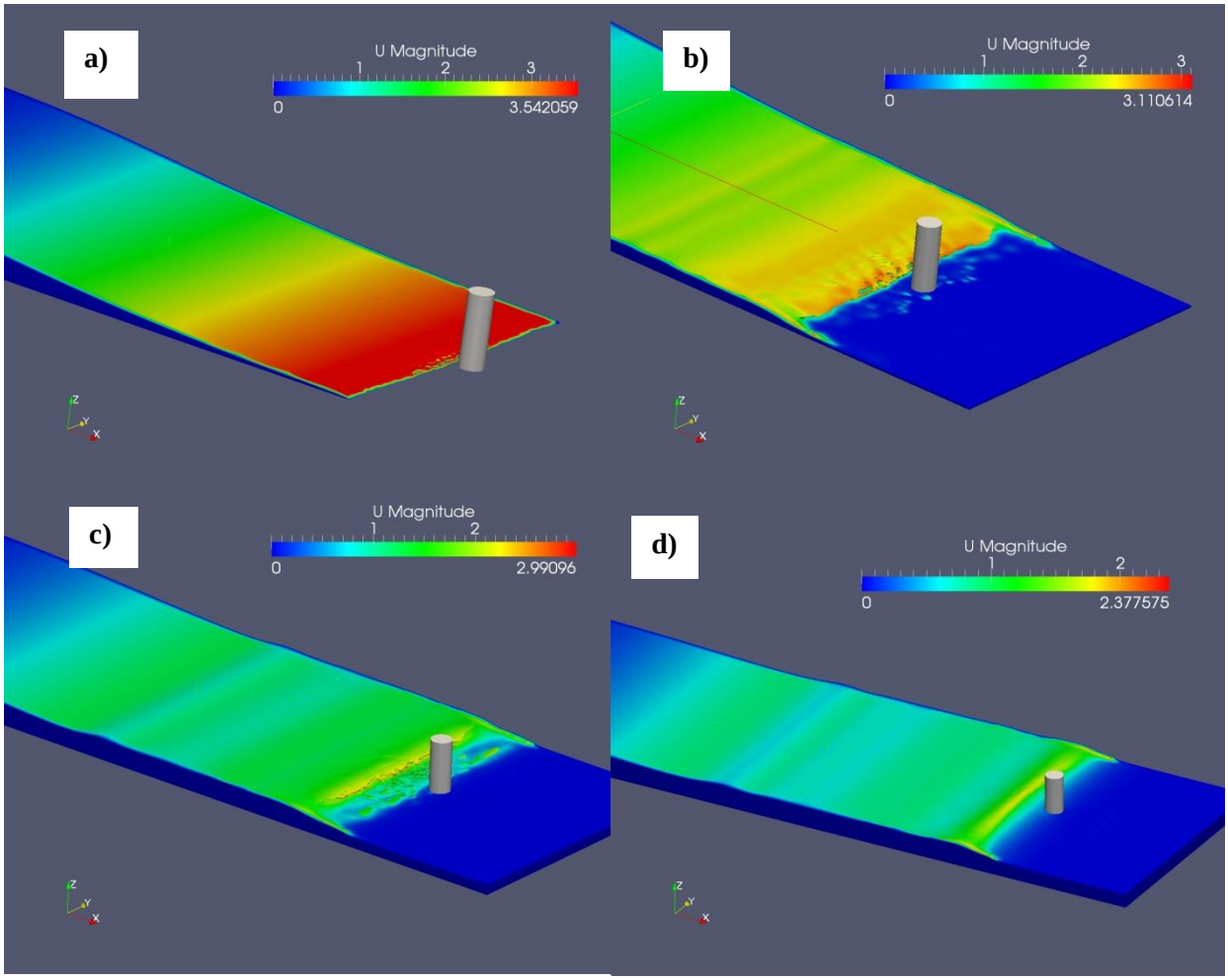

Fig. 13 Snapshots of bore impinging on the column during the impact time a) dry bed b) wet bed $h_d=0.05h_u$ c)wet bed $h_d= 0.3h_u$ d)wet bed $h_d=0.5h_u$

The bore development over different bed conditions before impact is displayed in Fig. 13. The undulation surface at the bore front is clearly observable for the case of the depth ratio h_d/h_u equal to 0.5. Furthermore, steeper bore fronts approach the column for all wet bed condition cases relative to the dry bed condition. Comparing the overall features of bore front for wet and dry bed conditions indicates the difference between the shapes of the bore front alongside of the width of the flume. Sequential wave trains appear in the cases with depth ratios of h_d/h_u as equal to 0.3 and 0.5. A slight form of an undulation surface is also observed for the depth ratio h_d/h_u as equal to 0.05.

In Fig. 14, the structure of the wake downstream of the columns is displayed for different bed conditions. Interestingly, the structure of the wake formation and the duration it takes to rejoin behind the column vary for different bed conditions. Basically, by increasing the downstream depth, the wake behind the structure forms faster. This duration was about 0.2sec, 0.3sec, 0.4sec and 0.6 after the bore impact for the depth ratios h_d/h_u=0.5, h_d/h_u=0.3, h_d/h_u=0.05 and dry bed, respectively. Moreover, no evidence of formation of a rooster tail was observed for any of the wet bed condition cases; however, this was visible for the dry bed, as shown in Fig. 14a. The split flows rejoined immediately downstream of the column for the wet bed conditions. In contrast, for the dry bed condition, the bore traveled about twice the diameter of the column and rejoined later downstream of the column. The same results were observed in St-

Germain et al.'s (2014) numerical results, in which the wake formation occurred faster in the case of a wet bed.

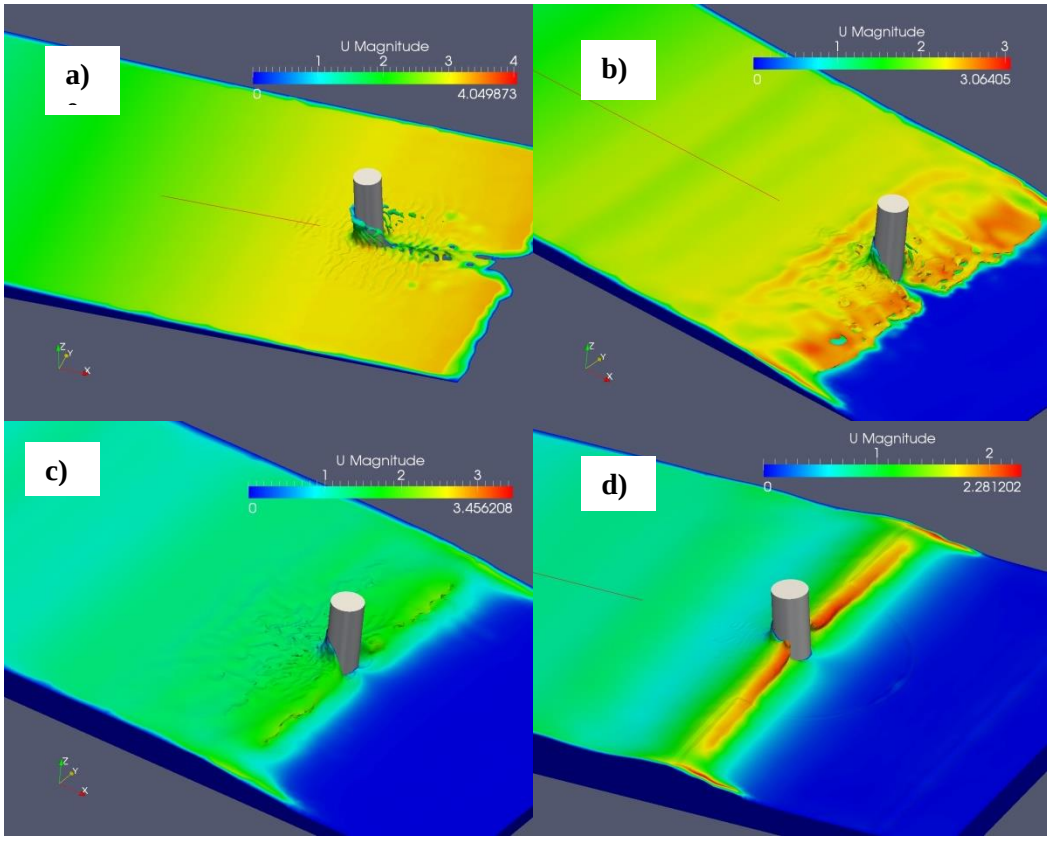

Fig. 14 Formation of wake downstream of the column for different bed conditions a) dry bed b) wet bed $h_d=0.05h_u$ c)wet bed $h_d= 0.3h_u$ d)wet bed $h_d=0.5h_u$

Furthermore, a comparison of the bore-front velocity vectors at the moment of impact is presented in Fig. 15, and a distinct difference between the velocity vectors can be observed. As the depth ratio increased, the higher velocities were more concentrated. In the case of the dry bed, the highest bore-front velocity as well as the lowest leading edge of the bore can be observed. This is also compatible with St-Germain et al.'s (2014) work. The authors observed a more elevated bore front in the case of wet bed conditions.

Although the bore front velocity decreased as the depth ratio (h_d/h_u) increased, greater depth and steepness of the bore front (as shown in Fig. 15) resulted in higher impulsive forces. The bore-front characteristics were altered substantially compared to the dry bed condition. Therefore, the subsequent impulsive and hydrodynamic forces are affected considerably, which will be discussed in Section 4.3.2.

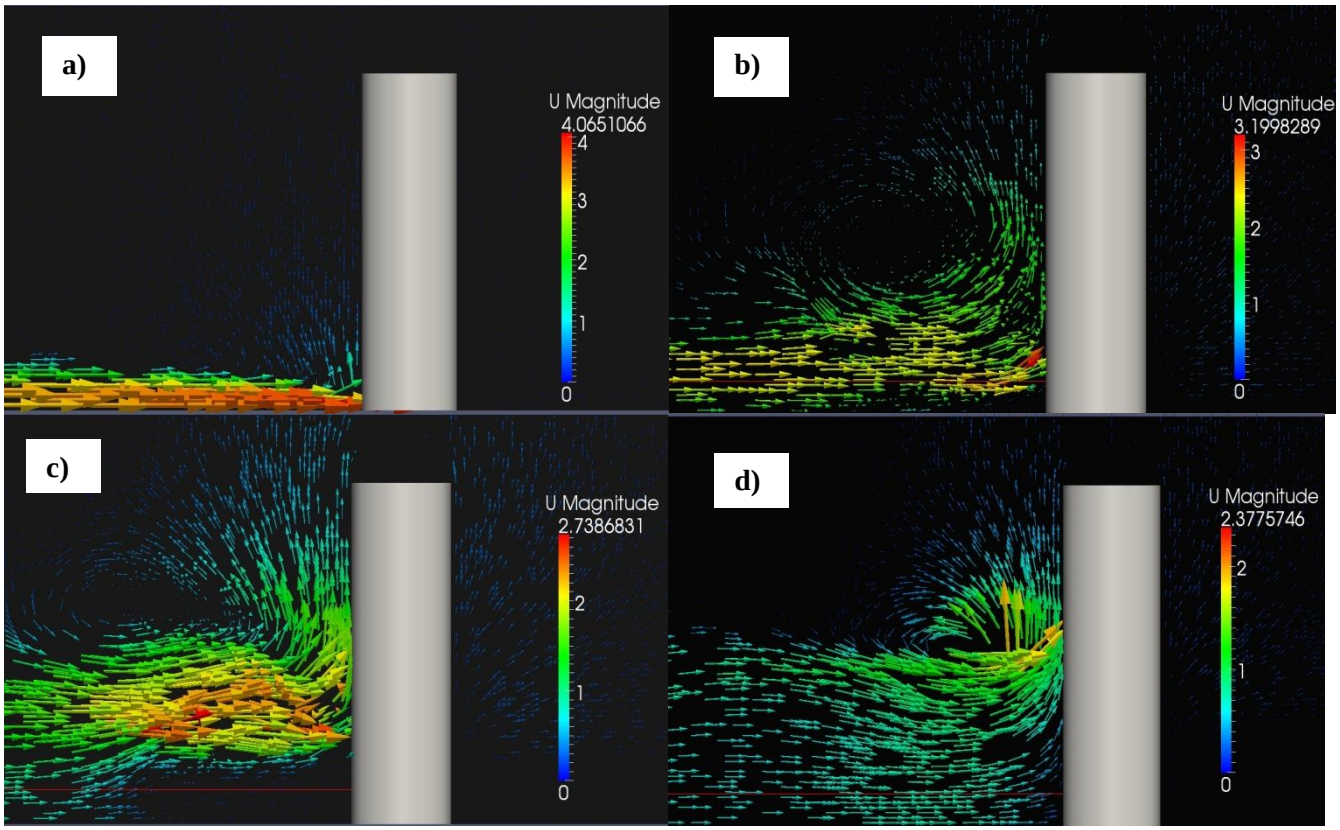

Fig. 15 Side view of velocity field upstream of the column at the flume centerline: a) dry bed; b) wet bed $h_d=0.05h_u$; c) wet bed $h_d= 0.3h_u$; d) wet bed $h_d=0.5h_u$

4.3.2. Resulting forces and pressures

For all bed conditions, the time-histories of the stream-wise forces exerted on the column are displayed in Fig. 16. The comparison between the wet bed cases with higher downstream depths of h_d/h_u as 0.3 and 0.5 with the dry bed condition and (lower downstream depth) wet bed of h_d/h_u=0.05 shows a clear difference in the general trends for the resultant stream-wise force. Comparison between the cases of the dry bed and (lower downstream depth) wet bed conditions with the h_d/h_u=0.05 shows that the impulsive force increased for the wet bed condition. Moreover, the subsequent run-up force is also higher for the case of the wet bed condition with the h_d/h_u ratio as 0.05. A similar higher impulsive force for the wet bed condition was also obtained by Ramsden (1993), who compared dry and bed conditions with initial impounded water depths of h_u=0.5m and h_d=0.028m.

Furthermore, after around 8 sec, the bed condition influenced the resulting stream-wise force. The maximum run-up was captured after 2.3 sec in the case of the dry bed condition. Despite the wet bed with a water depth ratio of h_d/h_u=0.5 showing a run-up higher than 60 cm, for the other tested cases, a run-up height of around 45cm was captured. Ramsden (1993) observed higher run-up elevations for the case of the wet bed condition compared with the dry bed. Owing to the circular shape of the column, a greater amount of flow was redirected around the column rather than splashing up on the upstream side. Similar results are also obtained for the bore run-up over the dry and wet bed conditions with an h_d/h_u ratio of 0.05. The run-up elevation for the wet bed condition is higher relative to that of the dry bed condition due

to a steeper and deeper bore front; however, after 2.5 sec the run-up elevations converge for the aforementioned cases.

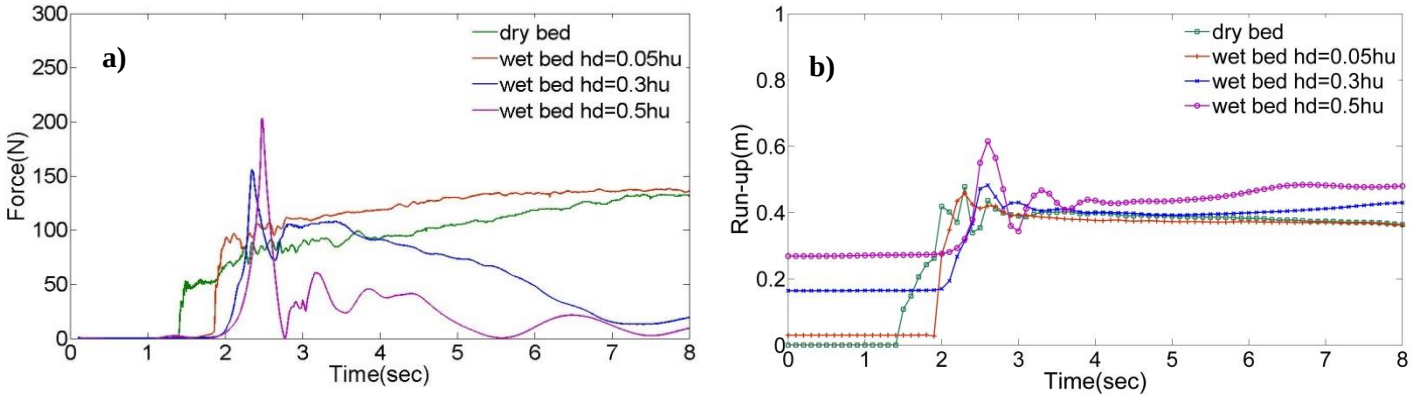

Fig. 16 Time histories of: a) Stream-wise force acting on the column for h_u=550mm; b) bore run-up on the upstream side of the column for h_u=550mm

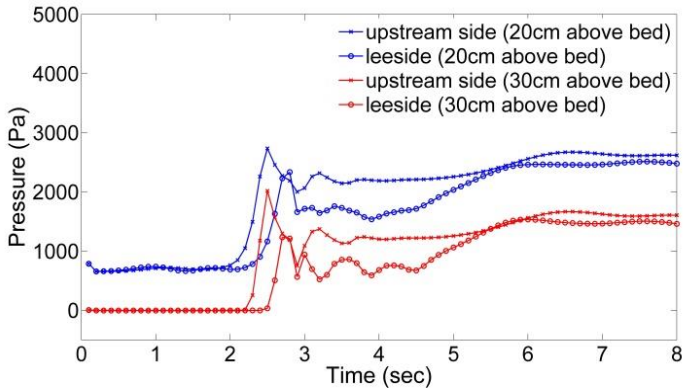

Fig. 17 Time history of pressure exerted on the column: upstream side (cross) and downstream (circle) of the column 20 cm (blue) and 30 cm (red) above the channel bed.

Comparison between the impulsive forces for wet bed conditions with h_d/h_u ratios equal to 0.3 and 0.5 shows a higher impulsive force for the ratio 0.5. This can be explained by the different bore front slopes and depths for these cases at the moment of impact (Fig. 16b). For the cases of wet beds with downstream to upstream ratios (h_d/h_u) equal to 0.3 and 0.5, a significant reduction in the resulting force can be observed in the quasi-steady state. This could be explained by the very slow flow velocity as well as the presence of still water around the column, which leads to a high level of hydrostatic pressure downstream of the column. In case of h_d/h_u=0.5, a force drop occurred immediately after impact (2.8sec), and the resultant force acting on the column was close to zero. To analyze the reason for this reduction, the time histories of pressure for the upstream and downstream sides of the column were measured at 20cm and 30cm above the channel, and are displayed in Fig. 17. Interestingly, the same values of pressure were obtained at this moment (2.8sec) at the upstream and downstream sides of the column. Afterwards, in the

quasi-steady state, the pressure differences upstream and downstream are negligible. This can explain the reduction in force values for h_d/h_u=0.5, which is substantial compared with the case of h_d/h_u =0.3. The other reason for the reduction in measured force (can also be seen in pressure) may be attributed to the high amount of air entrainment in the bore front for the case of h_d/h_u=0.5.

Moreover, Fig. 18 compares the time histories of the pressure at the upstream side of column. In the case of h_d/h_u = 0.5, the value of the impulsive pressure exceeded all other cases. This pressure may contribute to a high level of impulsive force for higher depth ratios; a higher portion of the pressure contributed on higher levels for the wet bed condition. At an elevation of 30 cm above the bed, still high values of pressure (more than 2000 Pa) were measured in the case of h_d/h_u = 0.5. A significant pressure drop at 2.8 sec (at the same moment corresponding to the time history of the force) can be observed in the pressure time history due to a high amount of air entrainment.

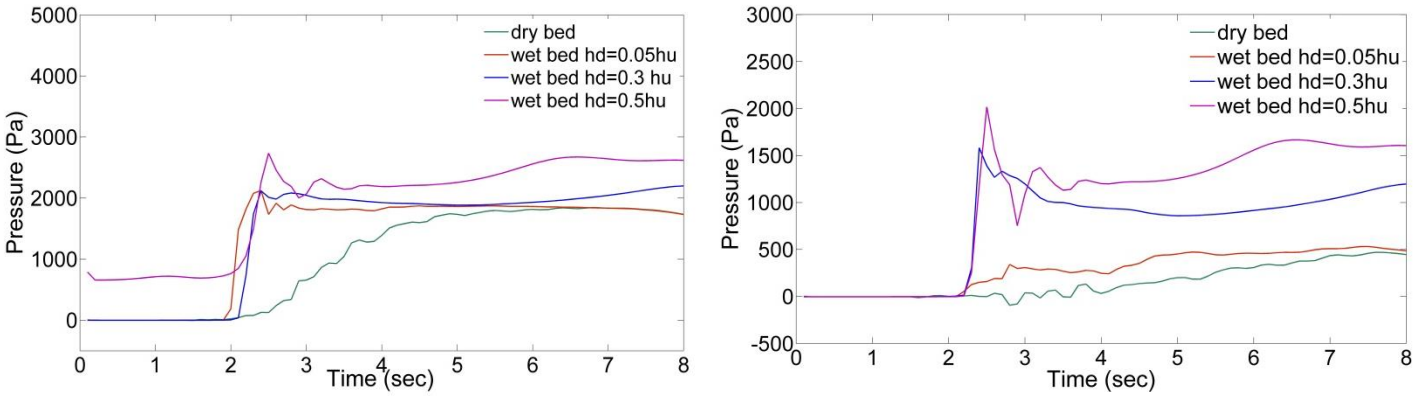

Fig. 18 Time histories of the pressure exerted on the upstream side of the column above the channel bed: a) 20cm; b) 30cm

4.3.3. Effects of bottom friction

The time histories of the stream-wise force exerted on the column are presented in this section. The simulations were performed for both smooth and rough beds, and the resulting force and bore depth-averaged velocities are shown in Fig. 19. In the case of the rough bed condition, the impulsive force decreases substantially. After approximately 6.0 sec, the force converged for the smooth and rough beds. The depth-averaged velocities are displayed in Fig. 19b. The bore front velocity and subsequent bore velocity are reduced due to energy dissipation induced by the bottom friction in the case of the rough bed. There is a marginal difference in force in the case of the asphalt and sand beds. Owing to lower velocities near the bed, a lower depth-averaged velocity was obtained in the quasi-steady state in the rough bed case.

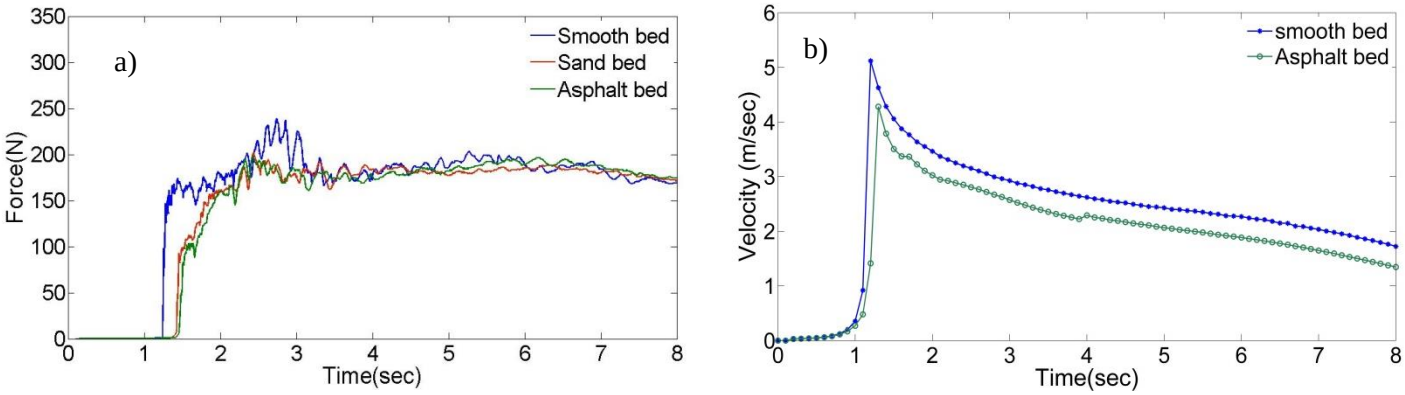

Fig. 19 Time histories of: a) stream-wise force exerted on the column; b) depth-averaged velocity (for smooth vs. rough bed for h_u=850mm impounded water depth)

5. Conclusion

A two-phase three-dimensional numerical model based on RANS equations (interFoam solver in OpenFoam) was used to investigate tsunami-like bore-structure interactions over different bed conditions (i.e., wet, dry and rough). Validation of the numerical model was performed with Nouri et al.'s (2010) experimental data. For the purpose of validation, the force and pressure exerted on the column as well as the bore surface elevation were compared between the numerical simulation and experimental measurements.

The major objective of the present study was to investigate the bore characteristics and forces exerted on structures over dry, wet and rough bed conditions. For this reason, a scaled-up model was used based on a validated numerical model for further simulation in order to eliminate the effects of sidewalls on the resulting forces. The numerical simulations for the dry bed were performed for circular and elliptical structures, and the bore evolution and the resulting force exerted on these columns were compared and analyzed. Moreover, the resulting force exerted on a circular column over dry and wet beds with downstream-to-upstream water depth ratios of 0.05, 0.3 and 0.5 are compared and the bore propagation characteristics investigated.

Based on the results, the bore front becomes steeper as downstream depth increases. This trend was also seen for the impulsive force, which could be attributed to corresponding steeper bore front as downstream depth increases. Further, during the quasi-steady state, a significant drop was seen for the hydrodynamic force in the case of higher downstream-to-upstream depth ratios (i.e., h_d/h_u of 0.3 and 0.5). The reason for this can be attributed to the high level of hydrostatic pressure downstream of the column. Moreover, the depth-averaged velocity was measured for all bed conditions, and significant reduction was observed as the depth ratio increased owing to the additional resistance induced by the downstream water depth. The establishment of a vortex in the wake of the structures differs with varying downstream bed conditions. The higher the depth ratio, the faster and closer the wake rejoined behind the column. The comparison of circular and elliptical columns over a dry bed demonstrated that the obtained impulsive force was substantially lower for the elliptical column. This could be due to the shape of the curvature at the very front of the elliptical column, which redirected the flow around the column rather than creating splash. The subsequent hydrodynamic force was later converged for both columns. In the present study, the influence of downstream depth on bore development and its propagation characteristics is revealed. The

major factor in this difference can be attributed to bore front steepness. The results support similar studies available in the literature.

References

Árnason, H. (2005). Interactions between an incident bore and a free-standing coastal structure. *Doctoral dissertation, Univ. of Washington*, Seattle, WA.

Árnason, H., Petroff, C., and Yeh, H. (2009). Tsunami bore impingement onto a vertical column. *J. Disaster Research*, 4(6), 391–403.

Berberovic, E., van Hinsberg, N.P., Jakirlic, S., Roisman, I.V., Tropea, C. (2009). Drop impact onto a liquid layer of finite thickness: dynamics of the cavity evolution. *Physical Review* E 79.

Chanson, H. (2006). Tsunami surges on dry coastal plains: application of dam break wave equations. *Coast. Eng. J*., 48(4), 355-370.

Chanson, H. (2009). Application of the method of characteristics to the dam break problem. *J. Hydraul. Res*., 47(1), 41-49

Chock, G., Robertson, I., Kriebel, D., Nistor, I., Francis, M., Cox, D. and Yim, S. (2011) Learning from Earthquakes The Tohoku, Japan, Tsunami of March 11, 2011: Effects on Structures. *EERI Special Earthquake Report.*

Crespo, A. J. C., Gómez-Gesteira, M., and Dalrymple, R. A. (2008) Modeling dam break behavior over a wet bed by a SPH technique. *J. Waterway, Port, Coastal, Ocean Eng*., 134(6), 313–320.

Dargahi. B. (1989), The turbulent flow field around a circular cylinder. *Experiments in Fluids,* 8 , pp1-12.

del Jesus, M., Lara, J.L., Losada, I.J. (2012). Three-dimensional interaction of waves and porous coastal structures. Part I: Numerical model formulation. *Coastal Engineering* 64, pp. 57-72.

Douglas, S., Nistor, I. (2015). On the effect of bed condition on the development of tsunami-induced loading on structures using OpenFOAM. *Natural Hazards,* 76(2), 1335-1356.

Earthquake Engineering Research Institute (EERI) [2011]. The Tohoku, Japan, tsunami of March 11, 2011: effects on structures, *Special Earthquake Report*.

Gómez-Gesteira M. and Dalrymple R.A. (2004). Using a three-dimensional smoothed particle hydrodynamic method for wave impact on a tall structure. *Journal of Waterway, Port, Coastal and Ocean Engineering*, 130(2),63–69.

Higuera, P., Lara, J.L., Losada, I.J. (2013). Realistic wave generation and active wave absorption for Navier–Stokes models: application to OpenFOAM. *Coast. Eng.*71, 102–118.

Janosi, I. M., Jan, D., Szabo, K. G., and Tel, T.(2004). "Turbulent drag reduction in dam-break flows."Exp. Fluids, 37, 219–229.

Kawamura, T., Mayer, S., Garapon, A., and Sorensen, L. (2002). Large Eddy Simulation of a Flow Past a Free Surface Piercing Circular Cylinder. *ASME J. Fluids Eng*., 124 , pp. 91–101.

Launder, B.E. and Spalding, D.B. (1974). The numerical computation of turbulent flows. *Computer Methods in Applied Mechanics and Engineering*, 3(2), 269–289.

Leal, J. G. A. B., Ferreira, R. M. L., and Cardoso, A. H. (2006). Dam-break wave-front celerity. *J. Hydraul. Eng.*, 132(1), 69–76

Menter, F. R. (1994). Two-equation eddy-viscosity turbulence models for engineering applications. *AIAA Journal* 32(8), 1598-1605.

Mikami, T., Shibayama. T., Esteban. M., and Matsumaru, R. (2012). Field survey of the 2011 Tohoku Earthquake and Tsunami in Miyagi and Fukushima Prefectures, *Coastal Engineering Journal*, 54(1), Special Issue of 2011 Tohoku Tsunami.

Nouri, Y., Nistor, I. and Palermo, D. (2010). Experimental investigation of tsunami impact on free standing structures, *Coastal Engineering Journal*, JSCE, 52(1), 43-70.

Ramsden , J.D. (1996). Forces on a vertical wall due to long waves, bores, and dry bed surges. *J.Waterways,Port Coasts and Ocean Eng.*,122(3),134-141.

Rusche, H. (2002). Computational fluid dynamics of dispersed two-phase flows at high phase fractions. *PhD thesis, Imperial College*, London, UK.

Sadeque. M. A. F., Rajaratnam. N., and Loewen. M. R. (2008). Flow around Cylinders in Open Channels. *ASCE J. Eng. Mech.*, (08), 134(1): 60-71.

Stansby, P. K., Chegini, A., and Barnes, T. C. D.(1998). The initial stages of dam break flow. *J. Fluid Mech.*, 374, 407–424

St-Germain P, Nistor I, Townsend R (2012) Numerical modeling of the impact with structures of tsunami bores propagating on dry and beds using the SPH method. *International Journal of Protective Structures* 3(2), 221–255.

St-Germain, P., Nistor, I., Townsend, R., and Shibayama, T. (2014). Smoothed particle hydrodynamics numerical modeling of structures impacted by tsunami bores. *J. Waterway, Port, Coastal, Ocean Eng*., 140 (1), 66-81.

Stoker, J. J.(1957). Water waves: The mathematical theory with applications, *Wiley-Interscience*, New York.

Wei, Z., Dalrymple, R. A., Hérault, A., Bilotta, G., Rustico, E. and Yeh, H. (2015). SPH modeling of dynamic impact of tsunami bore on bridge piers. *J. Coastal Eng.* 104, 26–42.

Weller, H.G. (2008). A new approach to VOF-based interface capturing methods for incompressible and compressible flow. *Technical Report TR/HGW/04*, OpenCFD Ltd., 2008.

Wilcox, D.C. (1988). Re-assessment of the scale-determining equation for advanced turbulence models. *AIAA Journal*, 26(11), 1299-1310.

Yeh, H., Sato, S. and Tajima., Y. (2013). The 11 March 2011 East Japan Earthquake and Tsunami: Tsunami Effects on Coastal Infrastructure and Buildings. *Pure Appl. Geophys*., 170, 1019-1031.

Yu G., Avital E. J., and Williams J. J. R. (2008). Large Eddy Simulation of Flow Past Free Surface Piercing Circular Cylinders. *ASME J Fluids Eng Trans* , 130, 10, pp. 41-49.